

Featuring work from the Laboratory of Applied Mechanobiology, Dirk Steuerwald, Susanna M. Früh, Rudolf Griss, Dr. Robert D. Lovchik and Prof. Viola Vogel, Department of Health Sciences and Technology, ETH Zürich, Switzerland.

Title: Nanoshuttles propelled by motor proteins sequentially assemble molecular cargo in a microfluidic device

The synergy of nanoshuttle-mediated active transport and pressure-driven passive transport in a microfluidic device enables the realisation of a molecular assembly line. Elaborate multistep protocols can be miniaturized into an autonomous working lab-on-a-chip device.

As featured in:



See Viola Vogel et al., *Lab Chip*, 2014, 14, 3729.



[www.rsc.org/loc](http://www.rsc.org/loc)

Registered charity number: 207890

# Nanoshuttles propelled by motor proteins sequentially assemble molecular cargo in a microfluidic device†

 Cite this: *Lab Chip*, 2014, 14, 3729

 Dirk Steuerwald,<sup>a</sup> Susanna M. Früh,<sup>a</sup> Rudolf Griss,<sup>‡a</sup> Robert D. Lovchik<sup>ab</sup> and Viola Vogel<sup>\*a</sup>

Nanoshuttles powered by the molecular motor kinesin have the potential to capture and concentrate rare molecules from solution as well as to transport, sort and assemble them in a high-throughput manner. One long-thought-of goal has been the realisation of a molecular assembly line with nanoshuttles as workhorses. To harness them for this purpose might allow the community to engineer novel materials and nanodevices. The central milestone towards this goal is to expose nanoshuttles to a series of different molecules or building blocks and load them sequentially to build hierarchical structures, macromolecules or materials. Here, we addressed this challenge by exploiting the synergy of two so far mostly complementary techniques, nanoshuttle-mediated active transport and pressure-driven passive transport, integrated into a single microfluidic device to demonstrate the realisation of a molecular assembly line. Multiple step protocols can thus be miniaturised to a highly parallelised and autonomous working lab-on-a-chip: in each reaction chamber, analytes or building blocks are captured from solution and are then transported by nanoshuttles across fluid flow boundaries in the next chamber. Cargo can thus be assembled, modified, analysed and eventually unloaded in a procedure that requires only one step by its operator.

 Received 28th March 2014,  
Accepted 24th June 2014

DOI: 10.1039/c4lc00385c

[www.rsc.org/loc](http://www.rsc.org/loc)

## Introduction

Since their early introduction, nanoshuttles have been envisioned as transporters for lab-on-a-chip applications.<sup>1–7</sup> To fulfill key tasks as molecular workhorses, the repertoire of nanoshuttle-cargo loading techniques and guiding strategies has been greatly expanded. Nanoshuttles have been used as powerful molecule transporters for molecular sorting,<sup>8–10</sup> surface imaging,<sup>11</sup> biosensing applications<sup>12–14</sup> and the assembly of supramolecular structures.<sup>13</sup> In a parallel effort, microfluidic systems have evolved over the past decades and substantial progress has been made in miniaturising and parallelising complex reactions in microfluidic devices.<sup>15–19</sup> It is thus time to combine these two approaches and their respective advantages. By exploiting the synergy of pressure-driven transport in a microfluidic device and active transport of nanoshuttles, we show the sequential assembly of molecular cargo.

In motor-driven nanoshuttle systems, microtubules are propelled by a carpet of surface-adsorbed kinesin motor proteins.<sup>20</sup> Each step that a kinesin-1 takes on the subunits of a microtubule is 8 nm long and consumes the energy provided by the hydrolysis of an ATP to an ADP molecule.<sup>21</sup> In this so-called inverted motility assay, which was first presented by Vale, Reese and Sheetz,<sup>22</sup> microtubules glide over the kinesin-coated surface at a defined distance of 13 nm.<sup>23</sup> Therefore, their motion can be monitored in real time by fluorescence microscopy.

The display of specific binding sites to load cargo is one of the prerequisites to load cargo to nanoshuttles, thereby enabling the engineering of novel materials and nanodevices with the help of active transport. Cargo pick-up has been demonstrated with a variety of molecules, biological entities and nanotechnological building blocks: amongst others, DNA,<sup>24–28</sup> viruses,<sup>29,30</sup> quantum dots<sup>31–36</sup> and other nanoparticles,<sup>10,34,37–39</sup> antibodies,<sup>13,14,30,40</sup> as well as lipid vesicles.<sup>41</sup> The most commonly used bond for cargo loading to actively drive microtubules is the protein–ligand interaction of streptavidin or neutrAvidin with biotin.<sup>10,13,24,25,27,28,30–36,38,39,41–46</sup> Alternative strategies utilise DNA hybridisation<sup>10,24,26,36,39,41,47</sup> and antibody–antigen interaction<sup>13,14,29,30,32</sup> as well as bioorthogonal covalent bonds.<sup>48</sup> Cargo unloading has been shown with DNA hybridisation<sup>39,41,47</sup> and DNA zipping and

<sup>a</sup> Laboratory of Applied Mechanobiology, Department of Health Sciences and Technology, ETH Zürich, 8093 Zürich, Switzerland. E-mail: [viola.vogel@hest.ethz.ch](mailto:viola.vogel@hest.ethz.ch)

<sup>b</sup> IBM Research GmbH, Säumerstrasse 4, 8803 Rüschlikon, Switzerland

† Electronic supplementary information (ESI) available: 3 videos, 7 figures and the calculations of shear stresses in this channel. See DOI: 10.1039/c4lc00385c

‡ Current address: Laboratory of Protein Engineering, EPFL Lausanne, 1015 Lausanne, Switzerland.



shearing geometries<sup>10</sup> as well as with a DNA restriction enzyme digest.<sup>36</sup>

Tight control of the direction of transport is equally important for future applications. Guiding of nanoshuttles has been realised using nanoscale kinesin tracks,<sup>49,50</sup> topographical elements<sup>1,8,51–57</sup> and shear flow<sup>58–60</sup> as well as with electric<sup>9</sup> and magnetic<sup>38</sup> fields. Motor proteins enable life far from thermodynamic equilibrium.<sup>10</sup> Not only are they able to transport the cargo against concentration gradients,<sup>10,61</sup> they also enable the transport of cargo in flow fields and across boundaries between laminar streams.<sup>8</sup> Taking advantage of these properties, we report the realisation of a fully functional molecular assembly line.

Our goal here was to combine pressure-driven flow in a microfluidic channel that contains four micro-reaction compartments with nanoshuttles that were actively propelled through these chambers which serve as mobile reaction platforms. Altogether five compartments – one shuttle landing stream and four micro-reaction compartments – have been realised by utilising the hydrodynamic separation of liquids in a microfluidic channel with low Reynolds numbers and the resulting laminar flow conditions:<sup>62</sup> five aqueous solutions containing different reaction components were divided by 4 stream boundaries. Biotinylated nanoshuttles served as an assembly platform onto which the 60-kDa protein neutrAvidin (NA) was loaded as a first cargo molecule (NA-cargo). The second cargo is a biotinylated single-stranded 40-nucleotide-long DNA (DNA-cargo). Both cargoes were fluorescently labelled. Therefore, we were able to observe the loading steps in real time on an area of 30  $\mu\text{m} \times 420 \mu\text{m}$ . The biggest challenge was to design a channel geometry in which the actively propelled nanoshuttles were able to pass the stream boundaries between the reaction chambers.

## Materials and methods

### Fabrication and operation of the microfluidic device

An image of the assembled chip is shown in Fig. S1† and the to-scale design plan is presented in Fig. S2.† The channel geometry was designed using the physical layout software L-Edit (Tanner EDA) and transferred onto a chromium mask. The structure was transferred onto a silicon wafer by photolithography with SU8-3025 photoresist. The 30- $\mu\text{m}$  broad channels were etched 40- $\mu\text{m}$  deep into silicon wafers by deep reactive ion etching (Bosch process). For the inlets and outlets, through-wafer vias (TWV) with a diameter of 100  $\mu\text{m}$  were etched through the 200- $\mu\text{m}$ -thick 4-inch silicon wafer using the same technique. To prevent clogging of channels, dust traps were integrated at every inlet. A 200  $\mu\text{m}$  thick 4 inch glass disk was anodically bonded onto the silicon wafer to yield a closed channel microfluidic network.<sup>63</sup>

Five PHD ULTRA syringe pumps from Harvard Apparatus were used in conjunction with five Hamilton TLLX 250  $\mu\text{L}$  syringes to each drive one flowing stream. The syringe pumps were run at individual flow rates of 0.1–1.5  $\mu\text{L min}^{-1}$  to generate a uniform flow profile for the five flowing streams

inside the sequential loading geometry: shuttle landing stream: 1.5  $\mu\text{L min}^{-1}$ , neutrAvidin (NA)-cargo loading stream: 0.9  $\mu\text{L min}^{-1}$ , DNA-cargo loading stream: 0.3  $\mu\text{L min}^{-1}$ , medium stream 1: 0.3  $\mu\text{L min}^{-1}$  and medium stream 2: 0.1  $\mu\text{L min}^{-1}$ . The syringes were connected to PE tubing (Instech Solomon, PA, USA) with an inner diameter of 584  $\mu\text{m}$ . This tubing was bonded to the microfluidic chip *via* nanoport assembly kits (Upchurch Scientific, WA, USA).

### Microtubule assembly

To assemble microtubules (MT) we adapted the standard protocol from Cytoskeleton, the provider of tubulin that was used here. Briefly, 20- $\mu\text{g}$  aliquots of both rhodamine-labelled tubulin (TL 331 M) and biotinylated tubulin (T 333-B, both from Cytoskeleton, CO, USA) were each dissolved to a concentration of 3.2  $\text{mg mL}^{-1}$  in BRB 80 buffer (80 mM PIPES, 2 mM  $\text{MgCl}_2$ , 1 mM EGTA, pH 6.85 with KOH) containing 4 mM  $\text{MgCl}_2$ , 1 mM guanosine 5'-triphosphate and 5% DMSO. These solutions were mixed in a ratio of 70% (vol) rhodamine-labelled tubulin to 30% (vol) biotin-labelled tubulin. After thorough vortexing, the solution was incubated on ice for 5 minutes in order to disassemble potentially polymerised microtubule fragments and achieve a homogeneous mixture of the two tubulin entities. Microtubules were then polymerised at 37  $^\circ\text{C}$  for 30 minutes and diluted 100-fold in BRB80 buffer containing 10 mM paclitaxel (taxol) for stabilising the biotin-rhodamine-labelled microtubules.

### Inverted motility assays integrated into microfluidic channels

Inverted motility assays were established and analysed on the glass surface that closes the microfluidic channel. At every step described below, solutions were flushed in from all five syringes to achieve a uniform surface coating in all five streams. To passivate the microfluidic channel and to minimise kinesin denaturation, a casein solution (1  $\text{mg mL}^{-1}$  casein in BRB80) was injected with a flow rate of 20  $\mu\text{L min}^{-1}$ . With no flow applied, the solution was incubated for at least 10 minutes to achieve a uniform surface coating with casein. Then the solution was exchanged with a solution containing the motor protein kinesin-1 (0.7  $\mu\text{g mL}^{-1}$  kinesin-1 in BRB80 containing 1  $\text{mg mL}^{-1}$  casein and 20 mM ATP). The kinesin-1 had been purified from *D. melanogaster* provided by Dr. Stephan Lakämper, ETH Zürich (purification described elsewhere<sup>21</sup>). This solution was injected at a lower flow rate of 10  $\mu\text{L min}^{-1}$  to prevent injury to the casein coating. After stopping the flow for no more than 10 minutes, the surface coating with kinesin was stopped in all five streams: in the NA-cargo loading stream, the DNA-cargo loading stream, medium stream 1 and 2 by injecting a motility solution (MS, which is BRB80 containing 0.4  $\text{mg mL}^{-1}$  casein, 10  $\mu\text{M}$  taxol, 10  $\mu\text{M}$  ATP and oxygen scavenging additives (20 mM D-glucose, 20  $\mu\text{g mL}^{-1}$  glucose oxidase type X-S from *Aspergillus niger*, 8  $\mu\text{g mL}^{-1}$  catalase, 10 mM dithiothreitol)) and in the shuttle landing stream by introducing 3.2  $\text{mg mL}^{-1}$  microtubules in MS at a flow rate of 10  $\mu\text{L min}^{-1}$ . After the kinesin

solution had been displaced several tens of seconds later, the flow rate was decreased to  $0.5\text{--}1\ \mu\text{L min}^{-1}$  in order to allow the microtubules to attach to the surface-adsorbed kinesin. Simultaneously, a steady flow was maintained in all five streams to prevent mixing of the consecutive laminar streams and to restrict microtubule landing to the shuttle landing stream. The binding of microtubules to the kinesin-functionalised surface was observed by confocal laser scanning microscopy (CLSM). As soon as a sufficient number of nanoshuttles had landed, the medium in the shuttle landing stream was exchanged for motility solution. All assays were conducted at room temperature.

### Sequential cargo loading to nanoshuttles

For cargo loading experiments, biotinylated MTs were first functionalised in the NA-cargo loading stream (Fig. 1) with motility solution containing 385 nM neutrAvidin Oregon Green 488 conjugate (Invitrogen A6374). The second cargo

molecule was applied in the DNA-cargo loading stream: a 40-base-long oligonucleotide functionalised with a biotin on the 3' end and a Cy5 label on the 5' end (sequence: TTT-TTT-AGC-TAT-TCG-AAC-TAT-AGC-TTA-AGG-ACG-TCT-TTT-T). The oligonucleotide was only able to couple to microtubules that had already loaded neutrAvidin molecules in the previous NA-cargo loading stream (see Fig. 2A). The oligonucleotide was applied to the nanoshuttles as a  $1\ \mu\text{M}$  solution in motility solution.

### Imaging

The inverted motility assays were observed with an Olympus FV 1000 Confocal Laser Scanning Microscope. For the visualisation of rhodamine labelled MTs, a 543 nm helium neon laser was used for dye excitation. The emission between 560 nm and 625 nm was monitored using either a  $40\times$  water immersion objective (NA = 0.9, Olympus PlanApo) or a  $60\times$  oil immersion objective (NA = 1.35, Olympus UPlanSApo). With the  $40\times$  water immersion objective, the pixel size was  $0.198\ \mu\text{m}$  per pixel and the optical resolution was  $0.335\ \mu\text{m}$ . The scan time was  $8\ \mu\text{s}$  per pixel. To excite the neutrAvidin-Oregon Green 488 conjugate, an argon laser with a wavelength of 488 nm was utilised. The wavelength window for detection was 500–560 nm.

A helium neon laser with a wavelength of 633 nm was applied to excite the Cy5 dye of the biotinylated DNA. All wavelengths longer than 640 nm reached the detector.

To properly differentiate between the three different fluorescence signals emitted and to eliminate crosstalk between them, the images presented were taken in sequential scanning mode.

### Image processing

The 3D reconstruction presented in video 1 in the ESI† and the projection in Fig. 1B were realised with the 3D/4D image processing and analysis software Imaris. Forty-four images for each of the three fluorescence channels were recorded by CLSM. The images were stacked using Imaris and then cropped to fit the selection marked with red lines in Fig. 1A. The black background was changed to white using Photoshop CS5.

The nanoshuttle trajectory in Fig. 2B was obtained by opening every third image of the recorded time lapse series (video 2 in ESI†) in the vector graphics editor Adobe Illustrator CS5 and tracing a single microtubule on each of these 23 images using the pencil tool and a line width of 3 DTP-points (pt). As a reference, a pre-drawn rectangle was copied into and aligned with the border of the image. The nanoshuttle traces and the rectangle were grouped and all of these groups were copied onto one image. The image was obtained by merging and colouring the three fluorescence channels with the image processing and analysis software ImageJ using the command “merge channels”. By aligning the rectangles with the border of this image, the nanoshuttle retraces were brought into place.

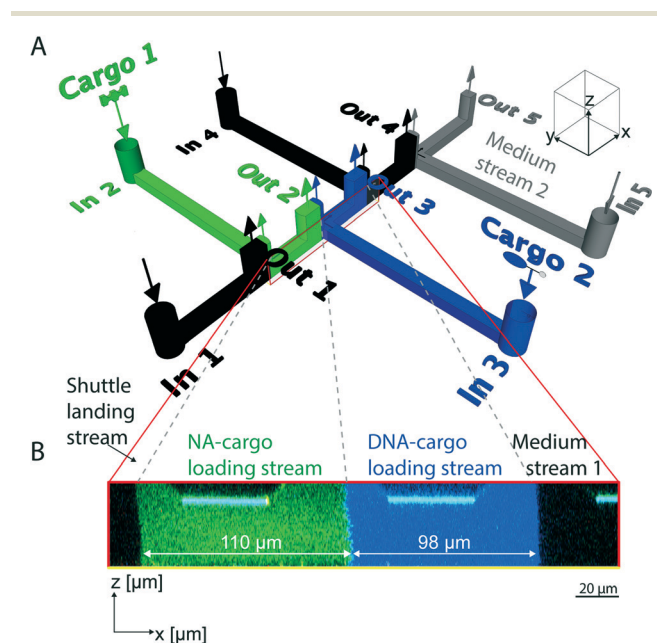


**Fig. 1** Overview of the channel geometry of the nanoshuttle assembly line. A: Sketch of the channel geometry with 5 inlets and 5 outlets as indicated by different colors to circulate different reagents (not to scale). Laminar flow conditions enable separation of the five landing and loading streams from each other by a sharply defined boundary layer. The detail marked with the red rectangle corresponds to the area depicted in (B) and Fig. 2A. B: Cross section of the operational channel along the  $x$ - $z$ -plane as marked by a red rectangle in (A). The  $z$ -stack utilized for this image has been built from 44 images that have been acquired with a confocal laser scanning microscope. The channel is closed at the bottom by a glass slide to which the kinesin motors are bound. The lid of the silicon channel appears as a horizontal line in light blue. Where this line is interrupted is where the outlet vias are etched through the silicon chip. The height of the channel is  $40\ \mu\text{m}$ . The NA-cargo loading stream (green) and the DNA-cargo loading stream (blue) obtain their colour from the fluorescent cargo they transport (green: NeutrAvidin Oregon Green 488 and false color blue: bio-ssDNA-Cy5). The shuttle landing stream and medium stream 1 appear in black. See also video 2 in the ESI.†

For the kymograph in Fig. 2C, the tip (in moving direction) of one nanoshuttle was traced with the segmented lines tool in the image processing software ImageJ. After finishing the line, the plugin “MultipleKymograph” was used to generate grayscale output images for each fluorescence channel with a line width of 1 pixel. The brightness and contrast of

these images were optimised; they were coloured by setting the lookup table to the corresponding colour. This is how the images “MT (Rhodamine) imaging channel”, “NA (Oregon Green 488) imaging channel” and “DNA (Cy5) imaging channel” were obtained. For the image “Overlay of MT, NA and DNA imaging channels”, the grayscale output images

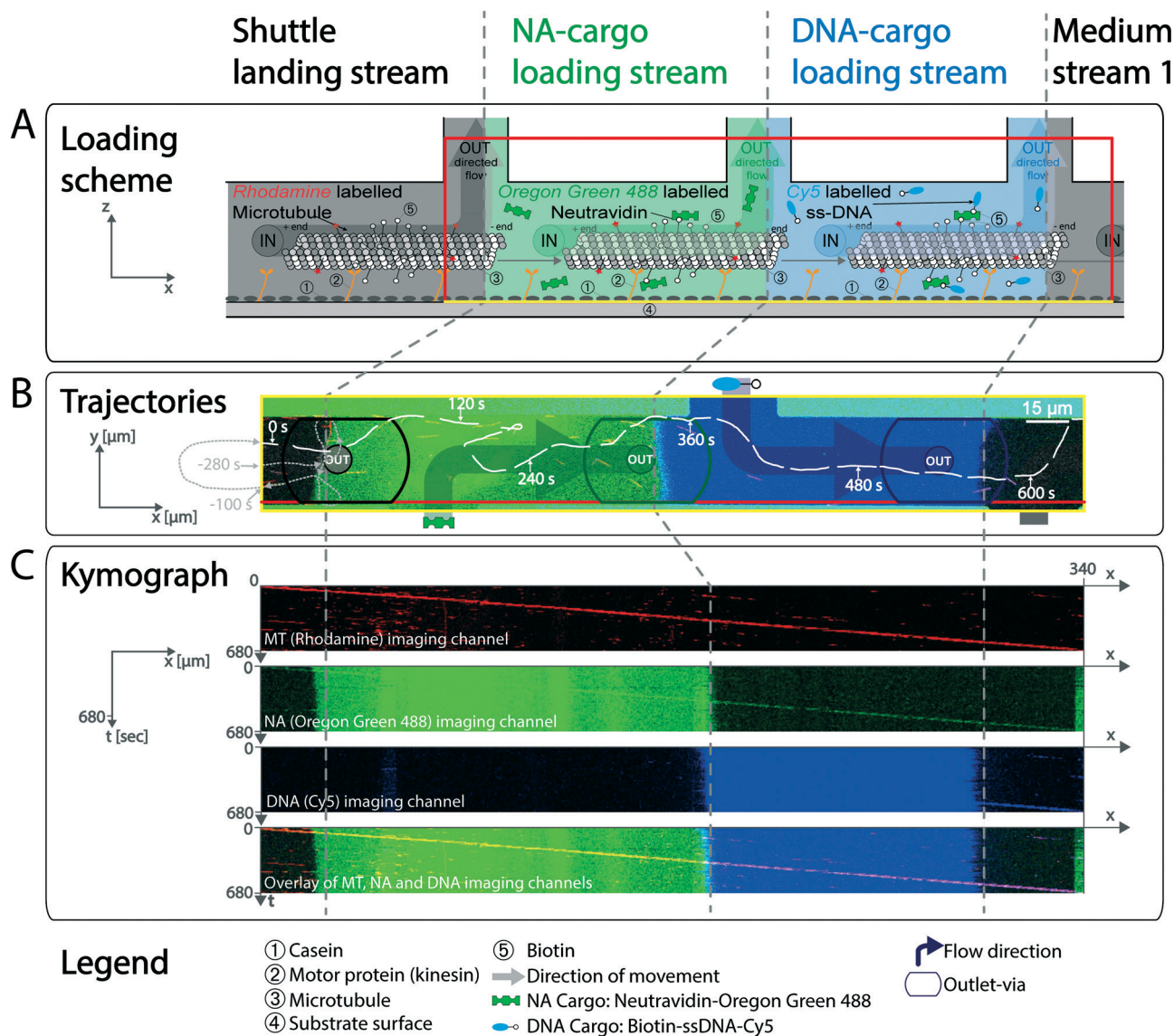


**Fig. 2** Visualization of the sequential assembly process driven by nanoshuttles. A: sketch of the loading scheme showing the functionalization of the glass surface with kinesins and microtubules as well as the sequential loading with cargo. In the shuttle landing stream, rhodamine and biotin bi-labelled microtubules land on the kinesin-coated surface. The nanoshuttles cross the border to the neutrAvidin (NA)-cargo loading stream and are loaded with Oregon Green 488 labelled NA that binds to the biotins. As soon as the microtubule crosses the border to the DNA-cargo loading stream, biotin-ssDNA-Cy5 cargo (false colored blue) is captured and transported. The area marked with the red rectangle corresponds to the one in Fig. 1A and B. The yellow line depicts the projection of the rectangle around the area in Fig. 2B, 3, S2B and S3B.† B: A representative nanoshuttle trajectory is depicted (white line), passing from the shuttle landing stream (black), through the NA-cargo (green) and DNA-cargo loading streams (blue) all the way to the medium stream 1 (black). The time gap between the positions is 30 seconds. The grey dotted line depicts the path of this particular nanoshuttle during the 280 seconds before  $t = 0$  s; it already entered the NA-cargo loading stream, captured the NA-cargo, left the field of view and re-entered at  $t = 0$  s; see also video 2 in the ESI.† C: time-lapse fluorescence kymograph of one microtubule moving through the four different loading streams. Each of the first three images shows the signal obtained from one fluorescence channel. The fourth picture is an overlay of these first three images. The first three images were generated by tracing the track of one particular nanoshuttle shown in Fig. 2B over 45 frames (frame rate 1 per 10 s). The time has been plotted on the y-axis; the distance has been plotted on the x-axis. The kymographs show how the nano-shuttle travels through all 4 streams of the microfluidic channel and how the cargo is loaded sequentially in the NA-cargo and the DNA-cargo loading streams.



from the “MultipleKymograph” were merged and coloured with the ImageJ command “merge channels”. Neither the input nor the output images of this step were optimised regarding their brightness or contrast.

The trajectories presented in Fig. 3 were drawn using the plugin MTrackJ for ImageJ. The velocity and distance measurements presented were calculated from these trajectories. Quantifying the parameters for Fig. 3, namely, stream crossings forward and backward, the number of MTs leaving the imaging plane as well as the number of returns into a subsequent stream were done by manually tracking and counting individual nanoshuttles.

## Results and discussion

### Operating nanoshuttles in microfluidic devices

To enable the active transport of nanoshuttles in the microfluidic device, the channel walls were coated with a casein solution to minimise motor denaturation, and then coated with the motor protein kinesin. Kinesin actively propels the microtubules forward, using ATP as an energy source.

Microtubules were then introduced into the first of five liquid streams, the shuttle landing stream (Fig. 1B and movie video 2 in the ESI†). Great care was taken to only let the microtubules land within the shuttle landing stream and that the ones that did not bind get washed out through the exit port of this stream. The goal was to ensure that all microtubules observed in subsequent stream compartments reached these downstream compartments only *via* active motor-driven

transport. To achieve this, the five streams were driven by the syringe pumps at all times so that the stream boundaries were efficiently separating the different microreaction chambers from each other.

Due to the fresh supply of ATP and oxygen scavenging reagents by the constant inflow of motility solution, the nanoshuttle system was long-lived in the microfluidic device and worked at very stable velocities.

### A microfluidic device with four micro-reaction compartments

To address the challenge to sequentially load actively propelled nanoshuttles with different types of cargo, a series of reaction compartments had to be designed through which nanoshuttles can actively transport their cargo across stream boundaries in a unidirectional manner. In the microfluidic channel geometry described here, five compartments – one compartment for shuttle landing and four micro-reaction compartments – have been established by utilising the hydrodynamic separation of liquids. The geometry comprises four intersections distributed on 360  $\mu\text{m}$  of the central channel (Fig. 1A and ESI† video 1). The channels are 30  $\mu\text{m}$  wide and 40  $\mu\text{m}$  thick. The total length of the channel, measured from all inlets to all outlets, is 35.7 mm. The resulting Reynolds numbers range between 0.05 (for 0.1  $\mu\text{L min}^{-1}$ ) and 0.71 (for 1.5  $\mu\text{L min}^{-1}$ ). The channels containing the NA-cargo and DNA-cargo loading streams are each 100  $\mu\text{m}$  long. These streams represent microreaction chambers for cargo loading, modification and unloading. The dust traps at each of the

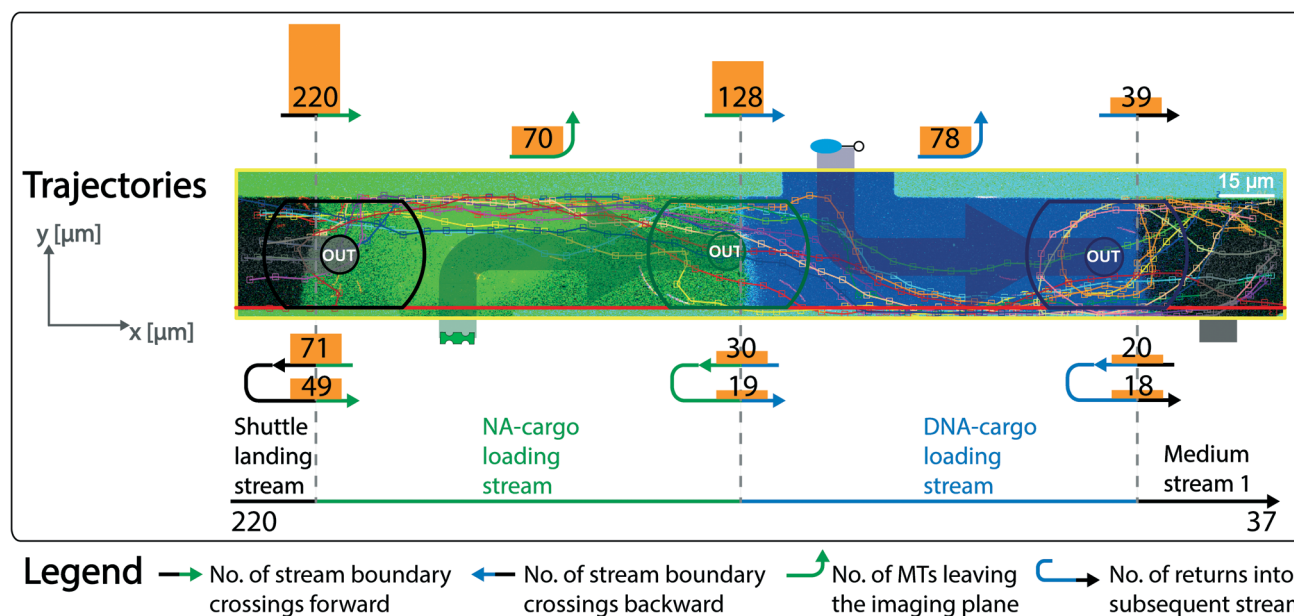


Fig. 3 Nanoshuttle trajectories through the device and quantification of stream boundary crossings. 220 nanoshuttles entered the field of view from the left and 37 of them made it all the way through the field of view. For the 10 of them, trajectories are shown in the image. For each stream boundary, we counted nanoshuttles, which succeeded in crossing (number of stream boundary crossings forward), how many turned around into the previous stream (number of stream boundary crossings backward) and how many of these moved again forward into the subsequent stream (number of returns into subsequent stream). For both cargo-loading streams (NA-cargo and DNA-cargo loading streams) the number of nanoshuttles that left the imaging plane was estimated (number of MTs leaving the imaging plane). The area marked with the yellow rectangle corresponds to the one in Fig. 2B, S2B and S3B;† the red line depicts the projection of the rectangle shown in Fig. 1A, B and 2A.

five inlets lowered the risk of channel clogging. The outlet ports of the presented geometry were deliberately placed in front of the intersections (Fig. 1B and 2B) to ensure the proper separation of aqueous streams throughout the cross section of the channel. In earlier-generation designs with vias placed right above the intersection, streams were leaking into the next one (see Fig. S4 and video 3 in the ESI†). The syringe pumps driving the microfluidic channel generated continuous flow rates of 0.1, 0.3, 0.9 and 1.5  $\mu\text{L min}^{-1}$ . By driving each stream from a different syringe pump, the flow rates could be adjusted individually to generate a uniform flow profile (Fig. 1B, 2B and video 1 in the ESI†). The streams had to be driven with different flow rates because of the backpressure in the channel geometry. With a length of about 160  $\mu\text{m}$ , the outlets of the shuttle landing, NA-cargo loading, DNA-cargo loading stream and medium stream 1 are comparably short. In contrast, with a length of about 5440  $\mu\text{m}$ , the outlet channel of medium stream 2 was designed to be rather long to allow for a long reaction time for future applications. As a consequence, the backpressure that was building up in the outlet channel of medium stream 1 was higher than those in the other four channels. Therefore, the flow rates had to be increased continuously from medium stream two towards the shuttle landing stream. A refined channel design would allow equal flow rates in every stream. While this is a proof-of-concept system, upscaling the design to more sophisticated or larger easy-to-fabricate geometries is possible as long as the laminar flow conditions are maintained.

### Guiding nanoshuttles across stream boundaries in the presence of orthogonal shear stresses

The prerequisite for establishing a molecular assembly line inside the presented microfluidic device is that the nanoshuttles move in only one direction and can pass across the subsequent boundaries between adjacent laminar streams and that only the non-bound nanoshuttles are washed away. Since shear stress directly guides nanoshuttles, as has been described before,<sup>58,59</sup> the escape of nanoshuttles from the central channel of the geometry through one of the outlets had to be prevented. Initially, our first generation designs had their in- and outlets on the same plane (see Fig. S5 in the ESI†). As a consequence, nearly all nanoshuttles followed the direction of flow into the first outlet before they had a chance to pass the boundary between the first two laminar streams.

Our second generation of devices was inspired by Kim *et al.*, who successfully guided nanoshuttles perpendicular to an applied flow field by utilising nanotracks made of CYTOP® on glass coverslips.<sup>8</sup> The tracks were roughly 250 nm high and 150 nm wide. In a related approach, we coated the surface of a channel geometry with inlets and outlets on the same plane with Teflon® nanotracks<sup>49</sup> to guide the nanoshuttles over the succeeding stream boundaries (ESI† Fig. S6). These Teflon® nanotracks were about 40–60 nm high and 800 nm–1  $\mu\text{m}$  wide. However, the guiding

force exerted by shear stress was stronger than the guiding capability of the Teflon® lines. In comparison to the CYTOP® nanotracks that Kim *et al.* had used, the Teflon® nanotracks were probably not high enough to efficiently guide the nanoshuttles through the flow field oriented perpendicular to the intended direction of the nanoshuttle movement. More detailed descriptions of these earlier approaches can be found in the ESI.†

To overcome the problem of nanoshuttles leaving the channel geometry with the first stream, the outlet vias were oriented vertically to the horizontally oriented channel network in the presented design. As a result of this, the liquid streams exit perpendicular to the plane of nanoshuttle movement. The only way for the microtubules to follow the flow profile of the stream and exit through one of the outlets would be to detach from the kinesin-coated surface. With this geometry, we were finally successful in efficiently guiding the nanoshuttles through the channel by shear stress acting at the bottom of the chambers but preventing the nanoshuttles from being detached from the surface. Since the five streams were driven with different flow rates, the shear stresses differed from compartment to compartment: a flow rate of 1.5  $\mu\text{L min}^{-1}$  in the shuttle landing stream corresponded to a shear stress of 15.8 Pa; a flow rate of 0.9  $\mu\text{L min}^{-1}$  in the NA-cargo loading stream corresponded to 9.5 Pa; a flow rate of 0.3  $\mu\text{L min}^{-1}$  in the DNA-cargo loading stream and medium stream 1 corresponded to a shear stress of 3.2 Pa; and a flow rate of 0.1  $\mu\text{L min}^{-1}$  in medium stream 2 corresponded to a shear stress of 1.1 Pa. Guided by these shear stresses, nanoshuttles were moving from the shuttle landing stream over the three subsequent stream borders all the way to medium stream 1 (Fig. 2B, C and video 2 in the ESI†). Taken together, this channel design made it possible to guide nanoshuttles across stream boundaries merely by shear stress and active transport – elaborate surface patterns were not necessary.

### Assessing the probability of how often nanoshuttles crossed stream boundaries

The trajectories for quantifying the unidirectionality and numbers for nanoshuttle take-offs have been generated by evaluating confocal fluorescence microscopy image sequences manually and with the plugin MTrackJ of ImageJ. The results are presented in Fig. 3. The number of motor-driven microtubule passages from the shuttle landing stream (black with red MTs) to the first NA-cargo loading stream (green) was 220. The number of nanoshuttles returning from the NA-cargo loading stream to the shuttle landing stream was 71 (32%). Of these nanoshuttles 49 (69%) made their way back from the shuttle landing stream to the NA-cargo loading stream. The probability of a unidirectional passage at the boundary between the shuttle landing and the first NA-cargo loading streams was thus 90%.

In the NA-cargo loading stream (green), 70 nanoshuttles disappeared from the imaging plane, either by leaving the

bottom of the channel by crawling up the sidewalls or by detaching from the surface. Therefore, 128 nanoshuttles could be tracked further and crossed the boundary between the NA-cargo loading (green) and the DNA-cargo loading streams (blue). 30 microtubules (23%) returned to the NA-cargo loading stream and 19 of these (63%) made their way back to the DNA-cargo loading stream. The unidirectionality at this stream border summed up to 91%.

In the DNA-cargo loading stream (blue), 78 nanoshuttles left the imaging plane. Therefore, 39 arrived at and crossed the boundary to stream 4. 20 microtubules (51%) returned to the DNA-cargo loading stream and 18 of these (90%) made their way back into medium stream 1. The unidirectionality at this border was 95%. The unidirectional transport efficiency across stream boundaries seems to correlate with two factors: first, the flow rate. It is known that guiding efficiency correlates with shear stress: the higher the shear flow, the more efficient is the nanoshuttle guiding.<sup>60</sup> In both DNA-cargo loading and medium stream 1, the shear stress of 3.2 Pa is relatively low. This might explain why the return rate is the highest at the boundary between DNA-cargo loading stream and medium stream 1: the stresses of 3.2 Pa in both of these streams provide only weak guiding and allow for a high rate of stream crossings backwards (51%). The second factor is related to our microchannel geometry: as mentioned above, the lengthy outlet channel of medium stream 2 causes a backpressure that builds up towards the shuttle landing stream. As a consequence of this, the stream boundaries were dislocated from their intended position (see Fig. S3†): for instance, the boundary between the NA-cargo loading and the shuttle landing stream was pushed back (upstream) 36  $\mu\text{m}$  into the NA-cargo loading stream. Therefore, a substantial volumetric portion of the NA-cargo loading stream leaves through the outlet of the shuttle landing stream and thereby exerts shear stress towards the left (see small arrows in Fig. S3 of the ESI†) and thus opposite to the intended direction of the nanoshuttle movement. We think that this contributes to a relatively high percentage (32%) of stream crossings backwards at this boundary. Optimising the channel design so that the flow rates are similar in each stream, mainly by shortening the outlet of medium, will also optimise the unidirectionality at the boundaries.

The number of microtubules passing through all four streams of the system was 39 (18%) of the 220 nanoshuttles that had entered the NA-cargo loading stream. The number of nanoshuttles passing through the channel can easily be increased using a higher microtubule concentration in the shuttle landing stream. We merely chose this low concentration to favour a better traceability of the nanoshuttles. By lowering the dilution, the parallelisation of reaction, concentration, assembly processes and others would be greatly enhanced.

We were able to trace 39 nanoshuttles from the shuttle landing stream to medium stream 1, which does not necessarily mean that the rest, *i.e.* 181 microtubules, were lost. It only indicates that 181 microtubules left the imaging plane.

A significant number of nanoshuttles have probably done this by moving up the sidewalls. A part of these shuttles might have anyway made their way to medium stream 1, either on the sidewall or by returning to the imaging plane. A possibility to prevent nanoshuttles from leaving the imaging plane is to engineer overhanging sidewalls, very much like done earlier, where overhangs prevented microtubules from crawling up the sidewalls of open channels.<sup>1</sup> A second reason for the high loss rate is most probably the take-off of microtubules from the kinesin-coated surface. Agayan *et al.* found that high shear stress facilitates the detachment of microtubules from the kinesin-coated surface.<sup>60</sup> Kim *et al.* suggested a gradual decrease in the surface density of microtubules in motility assays under flow.<sup>58</sup> They suggested a positive effect of supplementing the motility solution with the same concentration of kinesin that has been used to introduce kinesins to the device.<sup>58</sup> Even though we added kinesin-1 to the motility solution in a concentration of 0.7  $\mu\text{g mL}^{-1}$ , take-off events were quite frequent, especially near the stream borders. The reason for this was most probably that the flow direction right below the outlets is perpendicular to the moving plane of the nanoshuttles: in these regions, the stream exerts the highest lifting force onto the microtubules. The nanoshuttles detach from the surface as soon as the drag force exerted by the outlet flow is sufficiently high such that the swivelling microtubule tip is bent upwards and does not have a chance to reconnect with the surface-bound kinesins. At even higher forces, the microtubule–kinesin interactions can be zipped open – a single kinesin detaches above a force of 3 pN.<sup>60,64,65</sup> Another source of loss was the collision of nanoshuttles with walls or each other, which can result in buckling and eventually lift-off from the surface.<sup>55,56</sup>

### Proof of concept: a microfluidic assembly line that allows sequential cargo loading to nanoshuttles

Since the nanoshuttles succeeded in crossing three boundaries between the shuttle landing stream and the medium stream 1, we combined synergistic guiding with cargo loading to build a molecular assembly line. In the NA-cargo and DNA-cargo loading streams, the actively propelled transporters were exposed to cargo molecules, while the loading process was monitored online *via* fluorescence microscopy. To display the cargo loading process, one single nanoshuttle was tracked through the four streams, *i.e.* the shuttle landing stream, NA-cargo and DNA-cargo loading streams as well as medium stream 1 (Fig. 2B). The path of this nanoshuttle is depicted with 22 white lines. Each line was obtained by retracing the position of this very nanoshuttle at this very time point. The time gap between the positions is 30 seconds. The grey dotted line depicts the path of this particular nanoshuttle during the 280 seconds before  $t = 0$  s: it already entered the NA-cargo loading stream, captured the NA-cargo, left the field of view and re-entered at  $t = 0$  s. For Fig. 2C, the position and fluorescence readout for this nanoshuttle was mapped for each captured time point, beginning at  $t = 0$  s,



with the plugin “MultipleKymograph” for ImageJ. The resulting kymographs visualise how the NA- and DNA-cargoes were captured while passing through subsequent streams. As a proof of concept, we traced one single nanoshuttle (red) as it passed through the subsequent loading compartments and how it travelled all the way through the four streams (Fig. 2B and video 2 in ESI†). In the NA (Oregon Green 488) imaging channel (green), the emission of the dye on the neutrAvidin cargo is already visible in the shuttle landing stream. This is because the nanoshuttle had already entered the NA-cargo loading stream before  $t = 0$  s (see grey line in Fig. 2B). The signal of the Oregon Green 488 dye remains apparent for the rest of the observation. On its way through the NA-cargo loading stream, the cargo-loaded nanoshuttle is almost outshined by the strong background signal of free Oregon Green 488 dye in the stream. In the DNA imaging channel depicted in blue, the emission of the Cy5 dye coupled to the 40-base-long single-stranded oligonucleotide with a biotin on the 3' end (DNA-cargo) becomes visible only at the beginning of medium stream 1. This proves that the DNA-cargo is loaded from the DNA-cargo loading stream to the already neutrAvidin-functionalised transporters. Again, the cargo-loaded nanoshuttle is not visible on its way through the DNA imaging channel because it is outshined by the strong background signal of the free Cy5 dye in this stream. The fact that the DNA-cargo was coupled to the microtubules is also proof that neutrAvidin molecules had been loaded in the previous NA-cargo loading stream – because the biotinylated DNA-cargo can only be coupled to the nanoshuttles *via* the neutrAvidin “adapter” and because biotinylated cargo does not show unspecific binding to biotinylated microtubules, as shown earlier.<sup>66</sup> The signal for both the NA- and the DNA-cargo in medium stream 1 proves that a supramolecular cargo has been sequentially assembled on the nanoshuttle. The co-localisation of signals in the overlay of MT, NA and DNA imaging channels also clarifies this.

Since the microtubules travel at a constant distance above the surface,<sup>23</sup> the progress of the reaction can be visualised in real-time.

### Tuning the reaction time of shuttles with the cargo

The exposure time of nanoshuttles in a particular stream can be fine-tuned to suit the respective reaction or (un)loading kinetics. One approach is to adjust the length of a stream already when designing the channel. In our design, the length of both the NA-cargo and the DNA-cargo loading streams is 100  $\mu\text{m}$ . The effective length of the NA-cargo loading stream – from the boundary between the shuttle landing and the NA-cargo loading streams to the boundary between the NA-cargo and the DNA-cargo loading streams – measured 110  $\mu\text{m}$  (Fig. 1B). The effective length of the DNA-cargo loading stream was 98  $\mu\text{m}$  (Fig. 1B). The reason for the stream lengths to differ from the original design was the backpressure building from the lengthy outlet channel of medium stream 1 (see above); as a consequence of this,

altered flow rates resulted in the displacement of stream boundaries from the intended positions (see Fig. S3 of the ESI†). The majority of microtubules did not choose the direct, but an elongated, path through the channel (Fig. 3). Some even turned around and made a loop *via* the previous stream as discussed above (Fig. 3 and S3†).

To average the physical length of the paths that microtubules chose through the NA-cargo and DNA-cargo loading streams, 10 nanoshuttles were tracked. The average path length of these 10 filaments through the NA-cargo loading stream was  $117.6 \pm 4.7 \mu\text{m}$ ,  $6\% \pm 4.2\%$  longer than the effective length of the stream. The average path length through the DNA-cargo loading stream was  $108.5 \pm 6.3 \mu\text{m}$ ,  $9.7\% \pm 6.4\%$  longer than the effective stream-length.

The average exposure times of nanoshuttles to the NA-cargo and DNA-cargo loading streams were obtained evaluating 10 nanoshuttle trajectories. The average exposure time to the particular stream was 192 seconds in the NA-cargo loading stream and 191 seconds in the DNA-cargo loading stream. To determine the average velocity of nanoshuttles in the device at room temperature, 14 tracks with about 50 data points each were evaluated. Over the whole length of the field of view, we found an average velocity of  $0.56 \pm 0.036 \mu\text{m s}^{-1}$ . The constant velocity over the roughly 13-minute time course of the experiment was due to the supply of fresh ATP which fueled the kinesin movement by the permanent inflow of fresh motility solution. Here, we see a second knob to tune the exposure time, namely by taking a direct influence on the velocity of the microtubules by raising or lowering the ATP concentration<sup>45</sup> in a particular stream. Thus, the velocity of nanoshuttles moving in a particular microreaction chamber can be adjusted on demand and in real-time.

### Various methods are available to implement unloading

The device presented here, in which the sequential exposure of nanoshuttles to liquids of different compositions has been realised, is of course ideal not only for loading but also for unloading cargo. Various methods have been previously demonstrated.

Taira *et al.* demonstrated cargo unloading with restriction enzymes: quantum dots were coupled to nanoshuttles *via* 21-nts-long DNA that was enzymatically cleaved for unloading.<sup>36</sup> This technique should be easy to implement in a channel setup that allows for longer exposure times than ours does. Also, the method used by Hiyama *et al.* could be applied in our context: they bound the ssDNA-functionalised cargo to ssDNA-functionalised nanoshuttles *via* partial DNA hybridisation; the cargo was then transferred to the surface-bound unloading ssDNA due to complete and therefore stronger hybridisation.<sup>47</sup> This method established by Hiyama *et al.* could be transferred into our device by driving one of the streams with a solution containing the unloading ssDNA. This ssDNA would adsorb onto the surface to yield an unloading stream. Schmidt *et al.* demonstrated the loading and unloading of the cargo to and from nanoshuttles by DNA

hybridisation by exploiting mechanically weak and strong coupling geometries.<sup>10</sup> Unloading stations like these could be realised in our device as described above by adsorbing the unloading DNA from one of the stream liquids onto the surface of the channel. The cargo capture/release by malachite green presented by Hirabayashi *et al.*<sup>42</sup> would be another possibility to establish cargo unloading in the device presented here.

## Conclusions

A microfluidic platform has been developed that combines the advantages of two so far mostly complementary techniques: microfluidics and biological motor-driven active transport. In the prototypical microchannel design presented here, the long-thought-of dream of a sequential assembly line has been realised. Actively transported nanoshuttles are guided by shear flow across the sharp boundaries between five laminar streams in a well-controlled, sequential manner. Four of these streams represent microreaction chambers and the nanoshuttles guided through them serve as mobile reaction beakers. While passing through these chambers, the cargo is captured from solution, thereby concentrated and then transported across the stream boundary into the next stream. The boundaries represent highly efficient washing steps: nanoshuttles are actively transported across the boundary, take their captured cargo with them and thereby sort it, while unbound cargo can only pass this border by diffusion. The synergy of active transport and shear stress efficiently guides nanoshuttles on their way to assemble molecular building blocks in a short distance and makes elaborate surface topographies for guiding, loading and eventually unloading stations unessential. The system incorporates the intrinsic property for parallelising reaction, concentration, assembly processes and others, since many nanoshuttles pass through the channel in parallel. Here, the assembly of a supramolecular cargo has been demonstrated.

To further tune the platform for particular applications, several suggestions are listed below:

The number of chambers could be adjusted in the future to suit a particular application such as inserting additional modification steps for analyte tagging, shuttle or cargo modification as well as implementing an unloading reaction.

Since the channel design offers the possibility for the modular processing of molecular shuttles, one and the same device could prospectively first be used as a molecular assembly line and shortly afterwards as a sensor to analyse the product.

The system is already buffered for fragile proteins at a near-physiological pH of 6.9. Therefore, a wide variety of proteins and other biological entities can directly be used or studied without the need for buffer adjustments. The exposure time of nanoshuttles to a solution could in the future be fine-tuned by varying the ATP concentration<sup>45</sup> or channel length individually for each stream to maximise the collision probabilities and accommodate specific reaction kinetics.

One of the biggest advantages of the nanoshuttle system is that they are driven by ATP hydrolysis and can thus be operated autonomously from external power sources, as has been demonstrated by Bachand *et al.*<sup>14</sup> To preserve this property, the syringe pumps used in our setup could in the future be exchanged for on-chip capillary pumps<sup>67,68</sup> to manufacture yet completely autonomous devices.

We hope that our findings will impact a broad variety of interdisciplinary fields. Possible applications range from biosensors over the custom modification of biomolecules like proteins or DNA, the assembly of nanotechnological building blocks or the synthesis of small biomolecules, chemistry in labs-on-a-chip – especially in combination with the recently reported integration of “click chemistry” into the nanoshuttle system,<sup>48</sup> biotechnological prototyping reactions like modifying carbon nanotubes or synthesising custom DNA molecules, pharmacological testing of substances' impact on microtubules, or proteins of interest coupled to them, proteomics – on-line observation of protein interaction, kinetics or enzyme cascades to point-of-care diagnostics.

## Acknowledgements

Kinesin-1 was purified from *D. melanogaster* provided by Dr. Stephan Lakämper, ETH Zürich. Chromium mask development, silicon etching, wafer bonding and wafer dicing have been performed at the IBM Research Laboratory in Rüschlikon. We especially thank Ute Drechsler and Steffen Reidt for their most supportive help. Financial support from ETH Zürich is gratefully acknowledged.

## References

- 1 H. Hess, C. M. Matzke, R. K. Doot, J. Clemmens, G. D. Bachand, B. C. Bunker and V. Vogel, *Nano Lett.*, 2003, 3, 1651–1655.
- 2 D. Spetzler, J. York, C. Dobbin, J. Martin, R. Ishmukhametov, L. Day, J. Yu, H. Kang, K. Porter, T. Hornung and W. D. Frasch, *Lab Chip*, 2007, 7, 1633–1643.
- 3 A. Goel and V. Vogel, *Nat. Nanotechnol.*, 2008, 3, 465–475.
- 4 A. Agarwal and H. Hess, *J. Nanotechnol. Eng. Med.*, 2010, 1, 011005.
- 5 H. Hess and V. Vogel, *Rev. Mol. Biotechnol.*, 2001, 82, 67–85.
- 6 H. Hess, G. D. Bachand and V. Vogel, *Chem. – Eur. J.*, 2004, 10, 2110–2116.
- 7 T. Korten, A. Månsson and S. Diez, *Curr. Opin. Biotechnol.*, 2010, 1–12.
- 8 T. Kim, L.-J. Cheng, M.-T. Kao, E. F. Hasselbrink, L. Guo and E. Meyhofer, *Lab Chip*, 2009, 9, 1282–1285.
- 9 M. van den Heuvel, M. De Graaff and C. Dekker, *Science*, 2006, 312, 910–914.
- 10 C. Schmidt and V. Vogel, *Lab Chip*, 2010, 10, 2195–2198.
- 11 H. Hess, J. Clemmens, J. Howard and V. Vogel, *Nano Lett.*, 2002, 2, 113–116.
- 12 T. Fischer, A. Agarwal and H. Hess, *Nat. Nanotechnol.*, 2009, 4, 162–166.

- 13 S. Ramachandran, K.-H. Ernst, G. D. Bachand, V. Vogel and H. Hess, *Small*, 2006, 2, 330–334.
- 14 G. D. Bachand, H. Hess, B. Ratna, P. Satir and V. Vogel, *Lab Chip*, 2009, 9, 1661–1666.
- 15 P. N. Nge, C. I. Rogers and A. T. Woolley, *Chem. Rev.*, 2013, 113, 2550–2583.
- 16 E. K. Sackmann, A. L. Fulton and D. J. Beebe, *Nature*, 2014, 507, 181–189.
- 17 G. M. Whitesides, *Nature*, 2006, 442, 368–373.
- 18 T. Thorsen, *Science*, 2002, 298, 580–584.
- 19 P. Yager, T. Edwards, E. Fu, K. Helton, K. Nelson, M. R. Tam and B. H. Weigl, *Nature*, 2006, 442, 412–418.
- 20 J. Howard, A. J. Hudspeth and R. D. Vale, *Nature*, 1989, 342, 154–158.
- 21 D. L. D. Coy, M. M. Wagenbach and J. J. Howard, *J. Biol. Chem.*, 1999, 274, 3667–3671.
- 22 R. D. Vale, T. S. Reese and M. P. Sheetz, *Cell*, 1985, 42, 39–50.
- 23 J. Kerssemakers, J. Howard, H. Hess and S. Diez, *Proc. Natl. Acad. Sci. U. S. A.*, 2006, 103, 15812–15817.
- 24 S. Taira, Y.-Z. Du, Y. Hiratsuka, K. Konishi, T. Kubo, T. Q. P. Uyeda, N. Yumoto and M. Kodaka, *Biotechnol. Bioeng.*, 2006, 95, 533–538.
- 25 S. Diez, C. Reuther, C. Dinu, R. Seidel, M. Mertig, W. Pompe and J. Howard, *Nano Lett.*, 2003, 3, 1251–1254.
- 26 C. Z. Dinu, J. Opitz, W. Pompe, J. Howard, M. Mertig and S. Diez, *Small*, 2006, 2, 1090–1098.
- 27 R. Yokokawa, J. Miwa, M. C. Tarhan, H. Fujita and M. Kasahara, *Anal. Bioanal. Chem.*, 2008, 391, 2735–2743.
- 28 J. Miwa, M. Tarhan, H. Fujita, M. Kasahara and R. Yokokawa, *MEMS*, 2008, pp. 677–680.
- 29 G. D. Bachand, S. B. Rivera, A. Carroll-Portillo, H. Hess and M. Bachand, *Small*, 2006, 2, 381–385.
- 30 B. D. Martin, C. M. Soto, A. S. Blum, K. E. Sapsford, J. L. Whitley, J. E. Johnson, A. Chatterji and B. R. Ratna, *J. Nanosci. Nanotechnol.*, 2006, 6, 2451–2460.
- 31 J. Kerssemakers, L. Ionov, U. Queitsch, S. Luna, H. Hess and S. Diez, *Small*, 2009, 5(15), 1732–1737.
- 32 L. Rios and G. D. Bachand, *Lab Chip*, 2009, 9, 1005–1010.
- 33 G. Bachand, S. Rivera, A. Boal, J. Gaudio, J. Liu and B. Bunker, *Nano Lett.*, 2004, 4, 817–821.
- 34 M. Bachand, A. Trent, B. Bunker and G. Bachand, *J. Nanosci. Nanotechnol.*, 2005, 5, 718–722.
- 35 B. Nitzsche, F. Ruhnnow and S. Diez, *Nat. Nanotechnol.*, 2008, 3, 552–556.
- 36 S. Taira, Y.-Z. Du, Y. Hiratsuka, T. Q. Uyeda, N. Yumoto and M. Kodaka, *Biotechnol. Bioeng.*, 2007, 99, 734–739.
- 37 C. Brunner, C. Wahnes and V. Vogel, *Lab Chip*, 2007, 7, 1263–1271.
- 38 B. M. Hutchins, M. Platt, W. O. Hancock and M. E. Williams, *Small*, 2007, 3, 126–131.
- 39 S. Hiyama, R. Gojo, T. Shima, S. Takeuchi and K. Sutoh, *Nano Lett.*, 2009, 9, 2407–2413.
- 40 A. Carroll-Portillo, M. Bachand and G. D. Bachand, *Biotechnol. Bioeng.*, 2009, 104, 1182–1188.
- 41 S. Hiyama, Y. Moritani, R. Gojo, S. Takeuchi and K. Sutoh, *Lab Chip*, 2010, 10, 2741–2748.
- 42 M. Hirabayashi, S. Taira, S. Kobayashi, K. Konishi, K. Katoh, Y. Hiratsuka, M. Kodaka, T. Q. P. Uyeda, N. Yumoto and T. Kubo, *Biotechnol. Bioeng.*, 2006, 94, 473–480.
- 43 M. C. Tarhan, R. Yokokawa, C. Bottier, D. Collard and H. Fujita, *Lab Chip*, 2010, 10, 86–91.
- 44 A. Agarwal and H. Hess, *Prog. Polym. Sci.*, 2010, 35, 252–277.
- 45 H. Hess, J. Clemmens, D. Qin, J. Howard and V. Vogel, *Nano Lett.*, 2001, 1, 235–239.
- 46 C. Bottier, J. Fattaccioli, M. C. Tarhan, R. Yokokawa, F. O. Morin, B. Kim, D. Collard and H. Fujita, *Lab Chip*, 2009, 9, 1694–1700.
- 47 S. Hiyama, T. Inoue, T. Shima, Y. Moritani, T. Suda and K. Sutoh, *Small*, 2008, 4, 410–415.
- 48 S. M. Früh, D. Steuerwald, U. Simon and V. Vogel, *Biomacromolecules*, 2012, 13, 3908–3911.
- 49 J. Dennis, J. Howard and V. Vogel, *Nanotechnology*, 1999, 10, 232–236.
- 50 C. Reuther, L. Hajdo, R. Tucker, A. A. Kasprzak and S. Diez, *Nano Lett.*, 2006, 6, 2177–2183.
- 51 L. Cheng, M. Kao, E. Meyhofer and L. Guo, *Small*, 2005, 1, 409–414.
- 52 J. Clemmens, H. Hess, R. Doot, C. M. Matzke, G. D. Bachand and V. Vogel, *Lab Chip*, 2004, 4, 83–86.
- 53 L. Jia, S. G. Moorjani, T. N. Jackson and W. O. Hancock, *Biomed. Microdevices*, 2004, 6(1), 67–74.
- 54 S. G. Moorjani, L. Jia, T. N. Jackson and W. O. Hancock, *Nano Lett.*, 2003, 3, 633–637.
- 55 J. Clemmens, H. Hess, J. Howard and V. Vogel, *Langmuir*, 2003, 19, 1738–1744.
- 56 J. Clemmens, H. Hess, R. Lipscomb, Y. Hanein, K. Bohringer, C. Matzke, G. Bachand, B. Bunker and V. Vogel, *Langmuir*, 2003, 19, 10967–10974.
- 57 Y. Hiratsuka, T. Tada, K. Oiwa, T. Kanayama and T. Uyeda, *Biophys. J.*, 2001, 81, 1555–1561.
- 58 T. Kim, M.-T. Kao, E. Meyhofer and E. F. Hasselbrink, *Nanotechnology*, 2006, 18, 025101.
- 59 R. Stracke, K. J. Böhm, J. Burgold, H.-J. Schacht and E. Unger, *Nanotechnology*, 2000, 11, 52–56.
- 60 R. R. Agayan, R. Tucker, T. Nitta, F. Ruhnnow, W. J. Walter, S. Diez and H. Hess, *Langmuir*, 2013, 29, 2265–2272.
- 61 N. Hirokawa, Y. Noda, Y. Tanaka and S. Niwa, *Nat. Rev. Mol. Cell Biol.*, 2009, 10, 682–696.
- 62 T. M. Squires and S. R. Quake, *Rev. Mod. Phys.*, 2005, 77, 977–1026.
- 63 C. C. Tripathi, S. Jain, P. Joshi, S. C. Sood and D. Kumar, *Indian J. Pure Appl. Phys.*, 2008, 46, 738–743.
- 64 S. Klumpp and R. Lipowsky, *Proc. Natl. Acad. Sci. U. S. A.*, 2005, 102, 17284–17289.
- 65 M. J. Schnitzer, K. Visscher and S. M. Block, *Nat. Cell Biol.*, 2000, 2, 718–723.
- 66 C. A. Helm, W. Knoll and J. N. Israelachvili, *Proc. Natl. Acad. Sci. U. S. A.*, 1991, 88(18), 8169–8173.
- 67 T. Fischer, A. Agarwal and H. Hess, *Nat. Nanotechnol.*, 2009, 4, 162–166.
- 68 M. Zimmermann, H. Schmid, P. Hunziker and E. Delamar, *Lab Chip*, 2006, 7, 119–125.